Mechanism of ternary breakup in the reaction ^{197}Au + ^{197}Au at 15A MeV

Junlong Tian,[1,2] Xizhen Wu,[1,*] Zhuxia Li,[1,*] Kai Zhao,[1] Yingxun Zhang,[1] Xian Li,[3] and Shiwei Yan[3]
[1]*China Institute of Atomic Energy, P.O. Box 275(18), Beijing 102413, China*
[2]*College of Physics and Electrical Engineering, Anyang Normal University, Anyang, Henan 455000, China*
[3]*College of Nuclear Science and Technology, Beijing Normal University, Beijing 100875, China*
(Received 29 December 2009; revised manuscript received 30 September 2010; published 15 November 2010)

The mechanism of the ternary breakup of the very heavy system ^{197}Au + ^{197}Au at an energy of 15A MeV has been studied by using the improved quantum molecular dynamics model. The calculation results reproduce the characteristic features in ternary breakup events explored in a series of experiments; i.e., the masses of three fragments are comparable in size and the very fast, nearly collinear breakup of the colliding system is dominant in the ternary breakup events. Further, the evolution of the time scales of different ternary reaction modes and the behavior of mass distributions of three fragments with impact parameters are studied. The time evolution of the configurations of the composite reaction systems is also studied. We find that for most of the ternary breakup events with the features found in the experiments, the configuration of the composite system has two-preformed-neck shape. The study shows that those ternary breakup events having the characteristic features found in the experiments happen at relatively small impact parameter reactions, but not at peripheral reactions. The ternary breakup reaction at peripheral reactions belongs to binary breakup with a neck emission.

DOI: 10.1103/PhysRevC.82.054608 PACS number(s): 25.70.Mn, 02.70.Ss, 24.10.Lx, 24.75.+i

I. INTRODUCTION

Multifragmentation has been found to be a general phenomenon in intermediate-energy heavy-ion collisions. With decreasing incident energy, heavy-ion reactions will go to fusion fission or quasifission following a transiently formed composite nuclear system. At a certain energy region, a ternary breakup, in addition to the binary fission, becomes important when the composite system becomes very heavy. Thus, in a certain sense, it is a phenomenon in between the multifragmentation and fusion-binary fission undergone in very heavy reaction systems. The study of the ternary breakup could certainly deepen our understanding of the dynamics of heavy-ion collisions and test the theoretical model. Recently, a series of experimental studies on the ternary breakup of the Au + Au collision at 15A MeV were performed in 4π geometry using the multidetector array CHIMERA at the Laboratori Nazionali del Sud in Catania [1–4]. The first characteristic feature of the ternary reactions explored in these studies was that the masses of three fragments were comparable in size [1]. Later, the same group found that very fast, nearly collinear breakup of the colliding system is dominant in this kind of ternary breakup [2–4]. The features for the ternary breakup reactions explored in these experiments are completely different from the commonly known process of formation of light-charged particles that accompanies binary fission. In the following, we use the term "ternary breakup" for the ternary fission. In fact, the ternary fission with three mass-comparable fragments for very heavy systems has a long history of theoretical studies. Early theoretical considerations for the very heavy systems, such as U + U and Au + Au, were based on the framework of the liquid-drop model with extension of the two-center description of the nuclear shape to the three-center description [5] and the Los Alamos finite-range macroscopic dynamical model [6]. Both studies were static and concluded that the ternary fission with large-mass lightest fragments could happen only when strong two-body dissipation existed. By considering both the experimental finding and the theoretical studies performed for this ternary fission, it seems to be worthwhile for us to perform a microscopically dynamic study of the mechanism of the ternary breakup. In this work, we will first calculate the mass and angular distributions of three fragments in the ternary breakup of Au + Au collisions at 15A MeV and compare them with experiments to see if the feature explored in a series of experimental studies can be reproduced or not, and then perform a comprehensive study of the mechanism of the ternary breakup reactions.

The improved quantum molecular dynamics (ImQMD) model is adopted in this work. The ImQMD model has been successfully applied in the study of heavy-ion collisions at intermediate energies and the results, such as the charge distribution of products in reactions, the n/p ratio of emitted nucleons, the double ratio of the n/p ratio of emitted nucleons, etc., are in good agreement with the experimental data [7,8]. In addition, the ImQMD model has also been applied to heavy-ion collisions at energies near a barrier by making serious improvements [9,10]. In the model, both the nuclear mean field and the collision term allowing for nucleon-nucleon scattering, including Pauli blocking, are treated properly. Thus, in principle, the dissipation, diffusion, and correlation effects are all included without introducing any freely adjusting parameter. Using the ImQMD model, the Coulomb barriers for many reaction systems were well described [9], the fusion excitation functions for a series of fusion reactions, including neutron-rich projectile and target reactions, were well reproduced [10], and the capture cross sections of ^{48}Ca + ^{208}Pb and ^{48}Ca + ^{238}U were also calculated [11] and compared with experimental data. The charge distribution of

*lizwux@ciae.ac.cn

products in the central collisions of ^{197}Au + ^{197}Au at 35A MeV and the mass distribution of final fragments in 7.0A MeV ^{238}U + ^{238}U collisions were reproduced quite satisfactorily by the model [12,13]. Thus, the ImQMD model is appropriate to study the mechanism of the ternary breakup in Au + Au at 15A MeV.

The paper is organized as follows. In Sec. II the ImQMD model is briefly introduced. The mass number distributions of three fragments in a ternary breakup are calculated in Sec. III. At the same time, the mass asymmetry of the lightest fragment, with respect to the largest fragment and the intermediate fragment, are also studied. In Sec. IV, the mechanism of the ternary breakup in ^{197}Au + ^{197}Au at 15A MeV is investigated. The angular distribution of three fragments is presented and compared with experimental results. Finally, a short summary is given in Sec. V.

II. BRIEF INTRODUCTION OF THE ImQMD MODEL

For the reader's convenience, we first briefly introduce the ImQMD model. In the ImQMD model, the same as in the original QMD model [14–17], each nucleon is represented by a Gaussian wave packet,

$$\phi_i(\mathbf{r}) = \frac{1}{\left(2\pi\sigma_r^2\right)^{3/4}} \exp\left[-\frac{(\mathbf{r}-\mathbf{r}_i)^2}{4\sigma_r^2} + \frac{i}{\hbar}\mathbf{r}\cdot\mathbf{p}_i\right], \quad (1)$$

where $\mathbf{r}_i$ and $\mathbf{p}_i$ are the centers of the ith wave packet in the coordinate and momentum space, respectively. σ_r represents the spatial spread of the wave packet. The total N-body wave function is assumed to be the direct product of these coherent states. Through a Wigner transformation, the one-body phase-space distribution function for N-distinguishable particles is given by

$$f(\mathbf{r},\mathbf{p}) = \sum_i \frac{1}{(\pi\hbar)^3} \exp\left[-\frac{(\mathbf{r}-\mathbf{r}_i)^2}{2\sigma_r^2} - \frac{2\sigma_r^2}{\hbar^2}(\mathbf{p}-\mathbf{p}_i)^2\right]. \quad (2)$$

For identical fermions, the effects of the Pauli principle are discussed in Ref. [18]. The approximative treatment of antisymmetrization is adopted in the ImQMD model by means of the phase-space occupation constraint method [19]. The density and momentum distribution of a system read as

$$\rho(\mathbf{r}) = \int f(\mathbf{r},\mathbf{p})d^3p = \sum_i \rho_i(\mathbf{r}), \quad (3)$$

$$g(\mathbf{p}) = \int f(\mathbf{r},\mathbf{p})d^3r = \sum_i g_i(\mathbf{p}), \quad (4)$$

respectively, where the sum runs over all particles. $\rho_i(\mathbf{r})$ and $g_i(\mathbf{p})$ read as

$$\rho_i(\mathbf{r}) = \frac{1}{\left(2\pi\sigma_r^2\right)^{3/2}} \exp\left[-\frac{(\mathbf{r}-\mathbf{r}_i)^2}{2\sigma_r^2}\right], \quad (5)$$

$$g_i(\mathbf{p}) = \frac{1}{\left(2\pi\sigma_p^2\right)^{3/2}} \exp\left[-\frac{(\mathbf{p}-\mathbf{p}_i)^2}{2\sigma_p^2}\right], \quad (6)$$

where σ_r and σ_p are the widths of wave packets in coordinate and momentum space, respectively, and they satisfy the minimum uncertainty relation

$$\sigma_r\sigma_p = \frac{\hbar}{2}. \quad (7)$$

The propagation of nucleons under the self-consistently generated mean field is governed by Hamiltonian equations of motion,

$$\dot{\mathbf{r}}_i = \frac{\partial H}{\partial \mathbf{p}_i}, \quad \dot{\mathbf{p}}_i = -\frac{\partial H}{\partial \mathbf{r}_i}. \quad (8)$$

The Hamiltonian H consists of kinetic energy and the effective interaction potential energy:

$$H = T + U, \quad (9)$$

$$T = \sum_i \frac{\mathbf{p}_i^2}{2m}. \quad (10)$$

The effective interaction potential energy includes the nuclear local interaction potential energy and the Coulomb interaction potential energy,

$$U = U_{\rm loc} + U_{\rm Coul}. \quad (11)$$

$U_{\rm loc}$ is obtained from the integration of the nuclear local interaction potential energy density functional. The nuclear local interaction potential energy density functional $V_{\rm loc}[\rho(\mathbf{r})]$ is the same as that in Refs. [10,12,13], which reads

$$V_{\rm loc} = \frac{\alpha}{2}\frac{\rho^2}{\rho_0} + \frac{\beta}{\gamma+1}\frac{\rho^{\gamma+1}}{\rho_0^\gamma} + \frac{g_{\rm sur}}{2\rho_0}(\nabla\rho)^2 + \frac{C_s}{2\rho_0}[\rho^2 - \kappa_s(\nabla\rho)^2]\delta^2 + g_\tau\frac{\rho^{\eta+1}}{\rho_0^\eta}. \quad (12)$$

Here ρ, ρ_n, and ρ_p are the nucleon, neutron, and proton density, respectively, and $\delta = (\rho_n - \rho_p)/(\rho_n + \rho_p)$ is the isospin asymmetry. By integrating $V_{\rm loc}$, we obtain the local interaction potential energy:

$$U_{\rm loc} = \frac{\alpha}{2}\sum_i\sum_{j\neq i}\frac{\rho_{ij}}{\rho_0} + \frac{\beta}{\gamma+1}\sum_i\left(\sum_{j\neq i}\frac{\rho_{ij}}{\rho_0}\right)^\gamma + \frac{g_0}{2}\sum_i\sum_{j\neq i}f_{sij}\frac{\rho_{ij}}{\rho_0} + \frac{C_s}{2}\sum_i\sum_{j\neq i}t_it_j\frac{\rho_{ij}}{\rho_0}(1-\kappa_s f_{sij}) + g_\tau\sum_i\left(\sum_{j\neq i}\frac{\rho_{ij}}{\rho_0}\right)^\eta, \quad (13)$$

where

$$\rho_{ij} = \frac{1}{\left(4\pi\sigma_r^2\right)^{3/2}}\exp\left[-\frac{(\mathbf{r}_i-\mathbf{r}_j)^2}{4\sigma_r^2}\right], \quad (14)$$

$$f_{sij} = \frac{3}{2\sigma_r^2} - \left(\frac{\mathbf{r_i}-\mathbf{r_j}}{2\sigma_r^2}\right)^2, \quad (15)$$

and $t_i = 1$ and -1 for protons and neutrons, respectively. The Coulomb energy is written as the sum of the direct and the exchange contributions, the latter being taken into account in

TABLE I. The model parameter.

α (MeV)	β (MeV)	γ	g_0 (MeV fm^2)	g_τ (MeV)	η	C_S (MeV)	κ_s (fm^2)	ρ_0 (fm^{-3})
−356	303	7/6	7.0	12.5	2/3	32.0	0.08	0.165

the Slater approximation:

$$U_{\rm Coul} = \frac{1}{2}\int \rho_p(\mathbf{r})\frac{e^2}{|\mathbf{r}-\mathbf{r}'|} \times \rho_p(\mathbf{r}')d\mathbf{r}\,d\mathbf{r}' - e^2\frac{3}{4}\left(\frac{3}{\pi}\right)^{1/3}\int \rho_p^{4/3}\,d\mathbf{R}, \quad (16)$$

where ρ_p is the density distribution of protons of the system. The phase-space occupation constraint method and the system-size-dependent wave-packet width are the same as adopted in the previous version of the ImQMD model [9,10]. The parameters used are the same as those used in Refs. [11,12] (see Table I).

In this work, the procedure for making initial nuclei of projectile and target is similar to that in Refs. [9–12]. The binding energies and root-mean-square radii for ^{197}Au are required to be 7.92 ± 0.05 MeV/nucleon and 5.35 ± 0.2 fm, respectively. The stability of the pre-prepared initial nuclei is well tested. The pre-prepared nuclei are tested to determine if they satisfy the following requirements: their binding energies and root-mean-square charge radii maintain proper values required by the properties of initial nuclei with a very small fluctuation, and the bound nuclei evolve stably without spurious emission within 6000 fm/c. Figure 1 shows the time evolution of the binding energy and radius of the initial nucleus ^{197}Au. Only those that satisfy these requirements will be taken as the "initial nuclei" and are stored for usage in reaction simulations. For fragment recognition, we adopt the conventional coalescence model [20] widely used in the QMD model calculations, in which particles with relative momenta smaller than P_0 and relative distance smaller than R_0 are considered to belong to one cluster. Here, R_0 and P_0 are taken to be 3.5 fm and 300 MeV/c, respectively [21,22]. In this work, we create more than 4000 bombarding events for each small impact parameter (b = 0–6 fm), 7000 bombarding events for b = 7–9 fm, and at least 10 000 events for each large impact parameter (b = 10–12 fm) for the Au + Au reaction at an energy of 15A MeV.

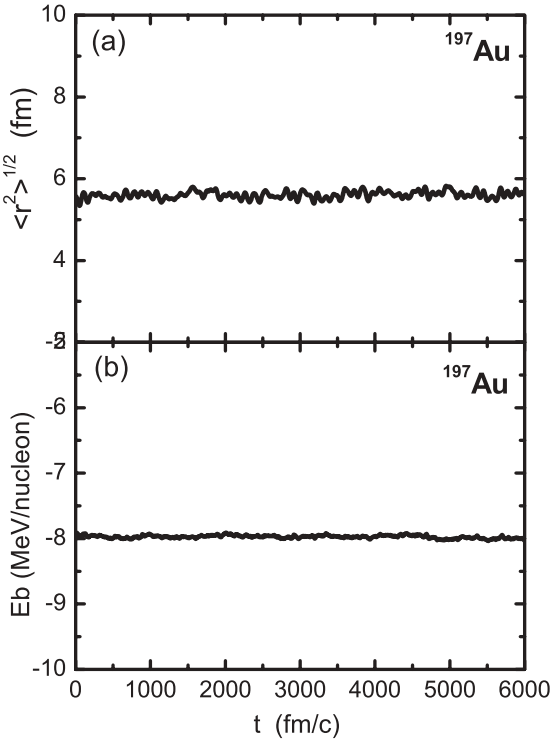

FIG. 1. The time evolution of the (a) root-mean-square radius and (b) the binding energy for ground states of ^{197}Au.

III. MASS DISTRIBUTIONS OF FRAGMENTS IN TERNARY BREAKUP REACTIONS

As in experiment [1], ternary events are selected under the condition of nearly complete balance of mass numbers allowing for up to 70 mass units, i.e.,

$$A_P + A_T - 70 \leqslant A_1 + A_2 + A_3 \leqslant A_P + A_T, \quad (17)$$

where $A_P + A_T$ is the total mass number and A_1, A_2, and A_3 are the masses of three fragments, respectively. Further, the conditions on the balance of longitudinal and transversal momentum applied in the experiment of Ref. [3] to make a further selection for the events in the calculations is also adopted in the event selection, $\|\sum_{i=1}^{3}\vec{P}_{\rm long}(i)\| > 0.8p_0$ and $\|\sum_{i=1}^{3}\vec{P}_{\rm trans}(i)\| < 0.04p_0$, where p_0 is the momentum of ^{197}Au projectiles. By counting the number of A_1, A_2, and A_3 masses at each impact parameter b, the production cross sections for A_1, A_2, and A_3 are obtained with the expression

$$\sigma(A_i) = 2\pi\int_0^{b_{\rm max}} bP(A_i,b)db, \quad (18)$$

where $P(A_i,b) = \frac{N(A_i,b)}{N_0(b)}$ is the production probability of fragment A_i with impact parameter b. $N(A_i,b)$ and $N_0(b)$ denote the number of fragments A_i produced in ternary events and the total ternary breakup events with impact parameter b. Here, $b_{\rm max}$ and Δb are 12.0 and 1.0 fm, respectively.

A. The mass number distributions for three fragments

First, we study the mass distributions of three fragments A_1, A_2, and A_3 in ternary events for ^{197}Au + ^{197}Au at an energy of 15A MeV. The results are shown in Fig. 2. Here, Fig. 2(a) is for A_1, Fig. 2(b) is for A_2, and Fig. 2(c) is for A_3. A_1, A_2, and A_3 are arranged according to the mass in a given event: A_1 the heaviest, A_2 the intermediate, and A_3 the lightest.

The histograms denote the experimental data taken from Ref. [1], and the lines with open circles are the results calculated with the ImQMD model. The experimental data and calculated results are both normalized for comparison. Figure 2 shows that the calculated results are in good agreement with

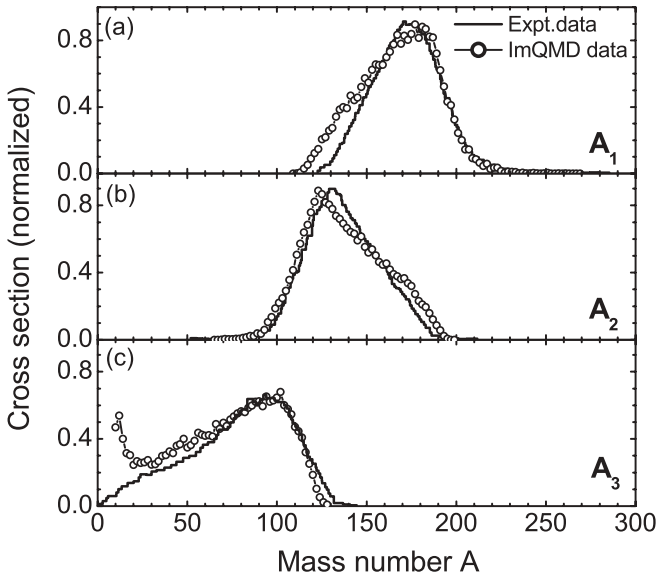

FIG. 2. Mass number distributions of (a) the heaviest A_1, (b) middle-mass A_2, and (c) the lightest A_3 fragments in selected ternary reactions of ^{197}Au + ^{197}Au at an energy of 15A MeV. The histograms denote the experimental data from Ref. [1] and the lines with open circles are the calculation results using the ImQMD model.

experimental data. The remarkable behavior shown in the mass distribution is quite different from the normal ternary fission appearing in the U, Pu, and Cf elements where only a small-size third fragment is accompanied with binary fission. It can be found that the mass difference of the most probable mass number of fragments A_2 with the mass of the projectile (or target) is about 60–70 mass units. Such a large mass difference seems difficult to explain by the normal nucleon transfer mechanism. This problem will be discussed later on. Now, we show the dependence of the average mass number

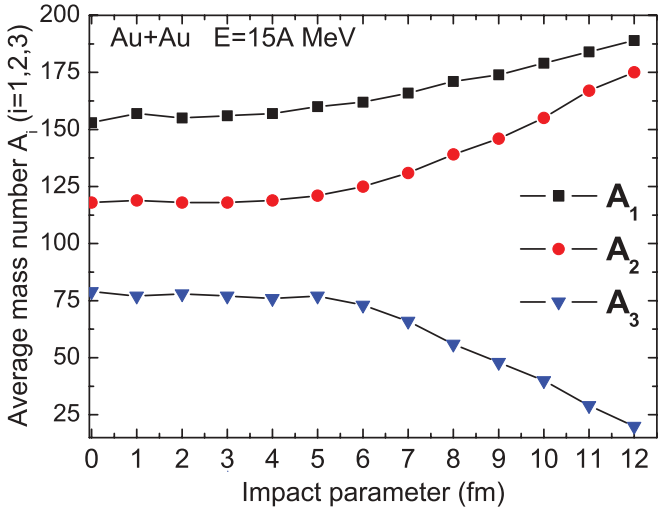

FIG. 3. (Color online) Impact parameter dependence of average mass numbers of fragments A_1 (solid squares), A_2 (solid circles), and A_3 (downward triangles) in select ternary reactions for the ^{197}Au + ^{197}Au system.

for each of three fragments on impact parameter in Fig. 3. This figure clearly shows that the ternary events with three mass-comparable fragments occur only at relatively small impact parameter collisions, which was also discussed in Ref. [4]. In peripheral collisions, less mass transfer occurs, and consequently, a small third fragment and two large-mass fragments (projectile-like or target-like) are produced.

B. Mass asymmetry of the third fragment with respect to two other fragments

In order to study the mechanism of mass transfer in the ternary breakup process, we investigate the mass asymmetry of A_3 with respect to A_1 and A_2, which may reflect spatial and temporal constraints in ternary reactions. We define $\eta_1 = (A_1 - A_3)/(A_1 + A_3)$ and $\eta_2 = (A_2 - A_3)/(A_2 + A_3)$. The probability distributions of mass asymmetries η_1 and η_2 at different impact parameters are shown in Fig. 4. First, we notice that for the cases of central and semicentral collisions (b = 0–6 fm), the probability distribution of η_1 shows a Wigner-like distribution [see Figs. 4(a) and 4(b)] with the most probable η_1 around 0.2–0.3, whereas for η_2, its probability distribution is like that of a Poisson-type distribution [see Figs. 4(e) and 4(f)]. This figure shows that A_3 and A_2 are likely to have a similar mass, while A_1 is most likely to be about 1.5–2 times larger than that of A_3 at relatively small impact parameters. However, from the point of view of probability theory, the Wigner- and Poisson-type distributions for η_1 and η_2 may reflect different spatial or temporal correlations between fragments A_1 and A_3, as well as between fragments A_2 and A_3. A Wigner distribution represents a certain correlation between objects under study. Contrarily, a Poisson distribution shows no correlation between objects under study. Whether there is a dynamical origin of Wigner- and Poisson-type distributions of η_1 and η_2 requires further study. Figures 4(d) and 4(h) represent the probability distributions of η_1 and η_2 at very large impact parameters b = 10–12 fm. The most probable η_1 and η_2 are both close to 1.0, and the corresponding probability distributions are almost the same. It is obvious that the third fragment produced in those events, as shown in Figs. 4(d) and 4(h), comes from the neck. The probability distributions shown in Figs. 4(c) and 4(g) are just between those in the cases just discussed.

IV. MODES AND MECHANISMS OF TERNARY BREAKUP IN ^{197}Au + ^{197}Au AT 15A MeV

To further understand the mass distribution and mass asymmetry in a ternary partition of ^{197}Au + ^{197}Au reactions at 15A MeV, in this section we study the modes and mechanisms of the ternary breakup reactions.

A. Two different modes of the ternary breakup reactions

First, we study the modes of the ternary breakup reactions. We suppose there are two time separations in a ternary breakup event. For convenience, we refer to the first time separation

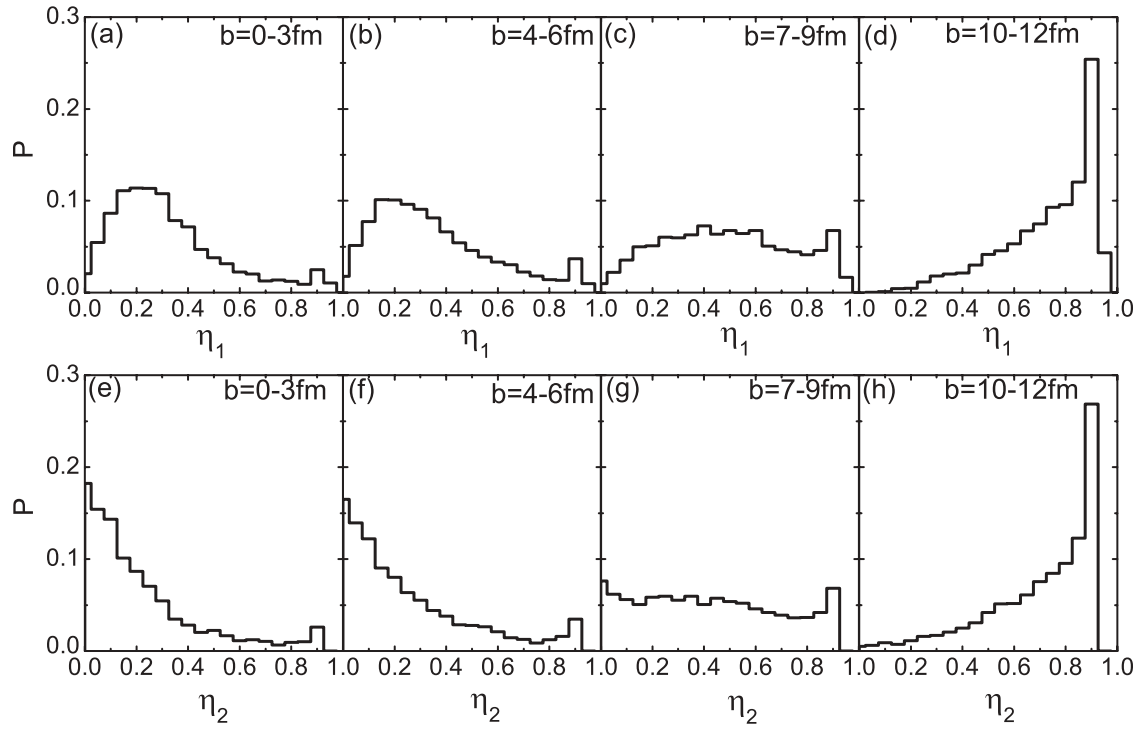

FIG. 4. The probability distributions of mass asymmetry η_1 (up) and η_2 (down) at impact parameters from $b = 0$ to 12 fm for ^{197}Au + ^{197}Au at 15A MeV.

as the first separation and the second time separation as the second separation. The time interval between these two separations is an important quantity used in the exploration of the mechanism of ternary reactions. To phenomenologically clarify the ternary breakup modes, as examples, we show snapshots of the time evolution of two typical ternary reaction events for ^{197}Au + ^{197}Au at 15A MeV in Figs. 5 and 6, respectively. The spatial configurations and time intervals between these separations are obviously different for these two events. For the event shown in Fig. 5, there exist two preformed necks and the time interval between the two separations is very short (less than 100 fm/c, which is the time step for recording the calculation results); during this interval the two necks break up almost simultaneously, and three fragments are formed from the composite system. This reaction mode is called the direct ternary breakup mode. The snapshot shown in Fig. 6 represents a typical cascade ternary breakup mode, for which the reaction process can be obviously divided into two steps. In the first step, the reaction system separates into projectile-like and target-like fragments, and in the second step, the projectile-like fragment (PLF) [or the target-like fragment (TLF)] breaks into two fragments and the complementary primary fragment survives. In this section, we mainly study these two breakup modes. Figure 7 shows the impact parameter dependence of the production probabilities for the direct and cascade ternary events in the reaction ^{197}Au + ^{197}Au at 15A MeV. One can see from the figure that the cascade mode is dominant in ternary breakup reactions at central and semiperipheral reactions. The probability for direct ternary reactions increases, and that for cascade ternary reactions decreases with impact parameters when $b > 6$ fm, and at very large impact parameters, the probability for direct ternary events exceeds that for cascade ternary events. It is clear that at very large impact parameters (peripheral reactions) the ternary breakup reaction is dominated by the binary breakup or binary process with simultaneously emitted light-charged particles at the neck. So, the increase of direct mode with impact parameter when $b > 6$ fm means that, in this case, the probability for a binary process with a neck emission increases with impact parameter.

B. Angular distribution of PLF breakup fragments

In Sec. IV A we showed that cascade ternary breakup events are dominant in relatively small impact reactions. Those events are definitely two-step reactions. In the first step, the reaction system breaks into a PLF and a TLF through deep-inelastic reactions and then, in the second step, either a PLF or a TLF breaks into two fragments and the complementary primary fragment survives and becomes the heaviest one. This scenario is in consistency with the distribution of η_1 and η_2 for the relative small impact parameter cases shown in Fig. 4. In order to make a comparison with the experimental results given in Refs. [2,4], only the events in which the second step is the breakup of the PLF are chosen and analyzed. Figure 8 shows the mass distributions of the PLFs and TLFs as well as the fragments F1 and F2 from the breakup of the PLF for the $b = 6$ fm case, for example. Here, the longitudinal velocity (in the laboratory system) of F1 is faster than that of F2. Indeed, one can see the scenario that the system first breaks into PLF and TLF with their mass distributions being of similar widths, and then the PLF breaks into two fragments, for

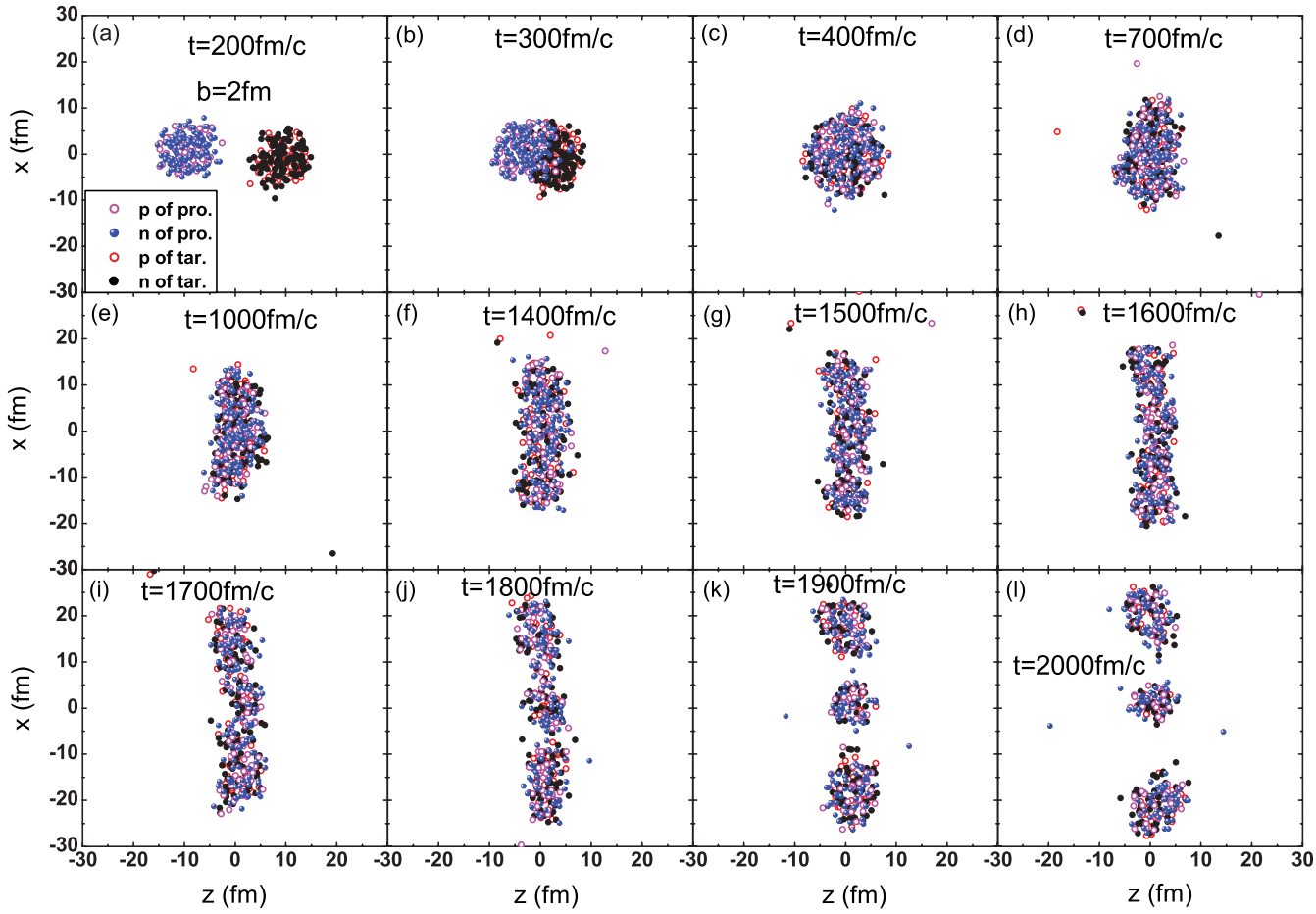

FIG. 5. (Color online) An example of direct ternary events for ^{197}Au + ^{197}Au at 15A MeV with $b = 2$ fm.

which the mass distribution widths are comparable. Further, we redefine the reaction plane by the beam direction and the separation axis of the PLF and the TLF, which is the direction of $\overrightarrow{V}_{\rm PT} = \overrightarrow{V}_{\rm PLF} - \overrightarrow{V}_{\rm TLF}$ with $\overrightarrow{V}_{\rm PLF}$ and $\overrightarrow{V}_{\rm TLF}$ being the velocities of the projectile and target in the laboratory system, respectively, the same as in Ref. [4]. The angle between the beam direction and $\overrightarrow{V}_{\rm PT}$ is written as $\theta_{\rm c.m.}$. The axis of the separation of the fragments produced in the breakup of the PLF is in the direction of $\overrightarrow{V}_{\rm F12} = \overrightarrow{V}_{\rm F1} - \overrightarrow{V}_{\rm F2}$. The angle between $\overrightarrow{V}_{\rm F12}$ and the normal of the reaction plane is written as θ and determines the out-of-plane angle of the PLF breakup axis and the azimuthal angle ϕ is the angle between $\overrightarrow{V}_{\rm PT}$ and the projection of $\overrightarrow{V}_{\rm F12}$ on the reaction plane. The out-of-plane angle θ, azimuthal angular distributions of fragments from PLF $\rightarrow$ F1 + F2 breakup, and the angle $\theta_{\rm c.m.}$ distribution are shown in Fig. 9. In order to make a comparison with the experimental results, the calculation results shown in Fig. 9 include contributions from reactions with a whole range of impact parameters ($b \leqslant b_{\rm max}$). The lines with solid circles are the calculated results using the ImQMD model. One can clearly see the distribution of θ peaks at 90°, which means the breakup of PLF is dominant in the plane. The azimuthal angular distribution of F1 sharply peaks at $\phi \sim 15°$ and the complementary fragments F2 peak at $\phi \sim -165°$. That is, the breakup axis of the PLF is very close to the breakup axis of the PLF and TLF. The calculation angular distributions of θ and ϕ show that the F1 and F2 produced in the breakup of the PLF and TLF are mostly in the same plane and nearly align along the TLF-PLF separation axis. For comparison, the experimental results are also shown in Fig. 9 by the lines with triangles [3]. One can see from the figure that our calculation results can reproduce the experimental results nicely, and the characteristic features of the ternary breakup reactions found in a series of experiments can be well exhibited by our model calculations. This tells us that the ImQMD model provides us with a desirable approach to the study of the mechanism of ternary breakup reactions.

C. The evolution of the time scale of the first and second separation with impact parameter

Now let us turn to the study of the evolution of the time scales of the first and second separations with impact parameters in the ternary reaction events. We define the first separation time as the time interval from the sticking time of two reaction partners to the first separation that occurs. Figure 10 shows the distributions of the first separation time for direct and cascade ternary events at $b = 2$, 7, and 10 fm,

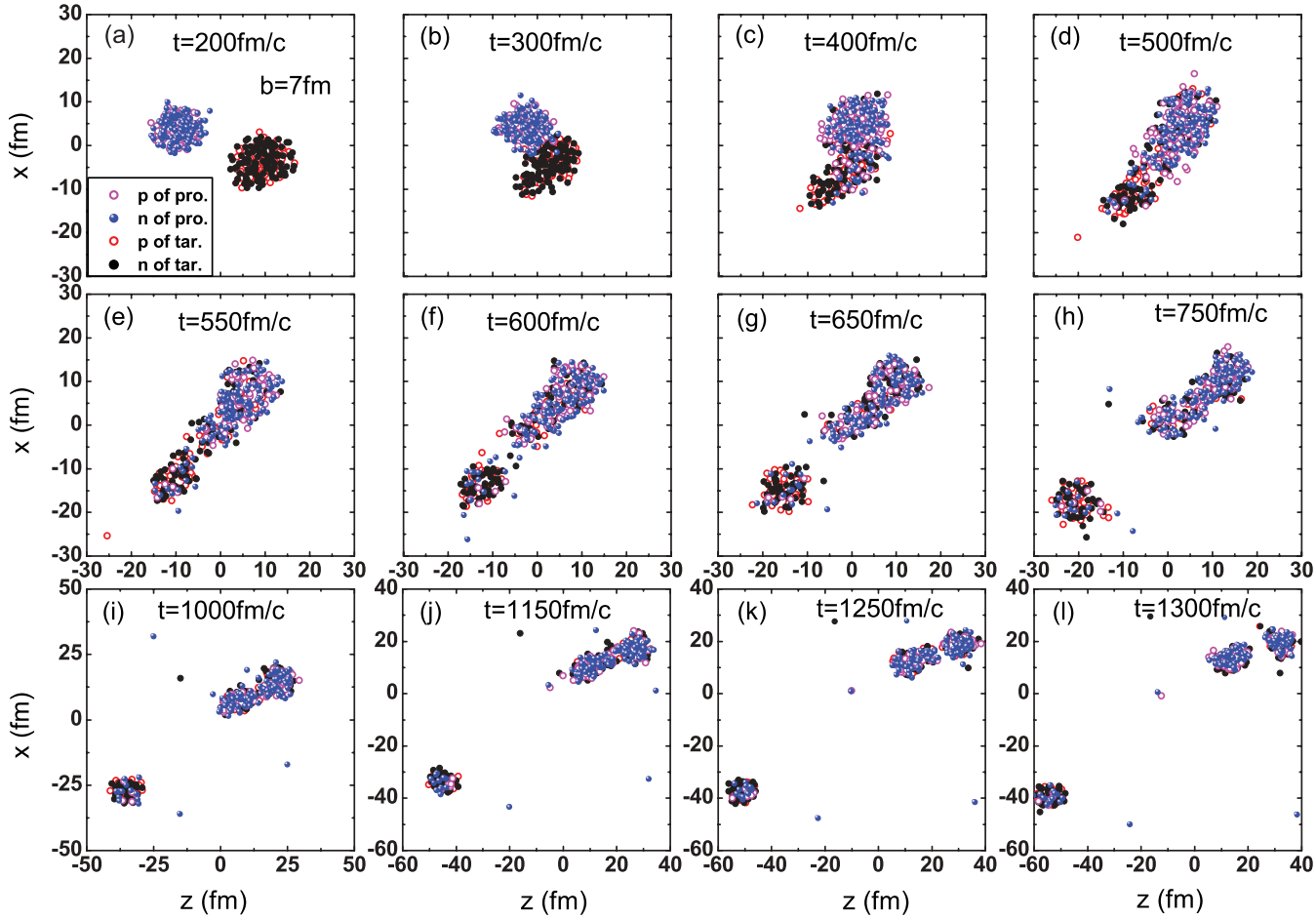

FIG. 6. (Color online) An example of a cascade ternary event for ^{197}Au + ^{197}Au at 15A MeV with $b = 7$ fm.

respectively. The top, middle, and bottom figures are for the cases where $b = 2$, 7, and 10 fm, respectively. The averaged first separation time for direct and cascade ternary events is also indicated in the figure. The top figure shows that the first separation for the direct ternary events mostly takes place later than those for the cascade ones in central collisions. The longer time scale of the first separation in the direct ternary events in central collisions means that in those events there is a longer interaction time between two reaction partners, and, consequently, the system has a longer time to rearrange nucleons to be in a lower energy configuration. Thus, two necks are preformed in the transiently formed composite system before the first separation takes place, as seen in Fig. 5. This kind of two-neck (or three-body-cluster) configuration is more favorable for reducing Coulomb repulsion. As the impact parameter increases, for instance, $b = 7$ fm, the first separation time quickly shortens and the difference in the first separation time between direct and cascade ternary events decreases, as shown in the middle figure, while in the case of $b = 10$ fm, the interaction time between reaction partners is short, and there are quite a few particles in the reaction zone. Consequently, the time scale of the first separation becomes short and the distributions of this time scale for two different ternary modes are almost the same, with only a small difference in the widths, as shown in the bottom figure.

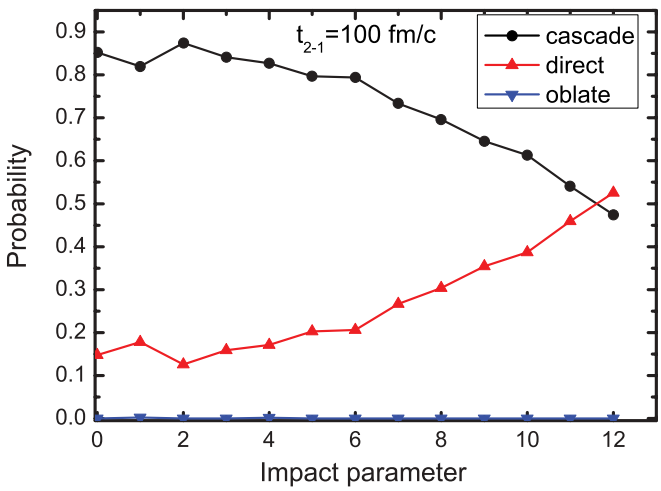

FIG. 7. (Color online) Impact parameter dependence of the probabilities for direct and cascade ternary events for ^{197}Au + ^{197}Au at 15A MeV. The line with downward triangles denotes direct oblate ternary events in which three fragments are emitted in a triangular shape. This only happens occasionally.

The study of the distribution of the time interval t_{2-1} between the first and second separation in ternary events is

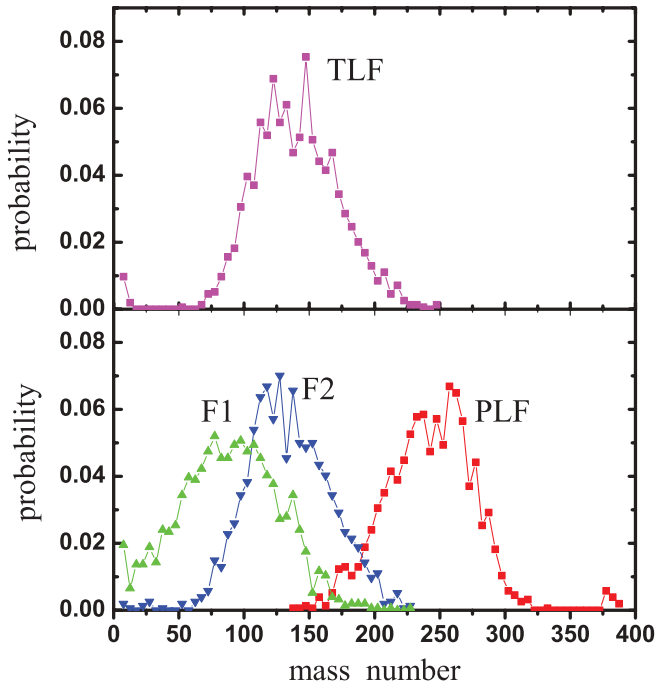

FIG. 8. (Color online) Mass distributions of the PLF and TLF and the fragments F1 and F2 from the breakup of the PLF at $b = 6$ fm.

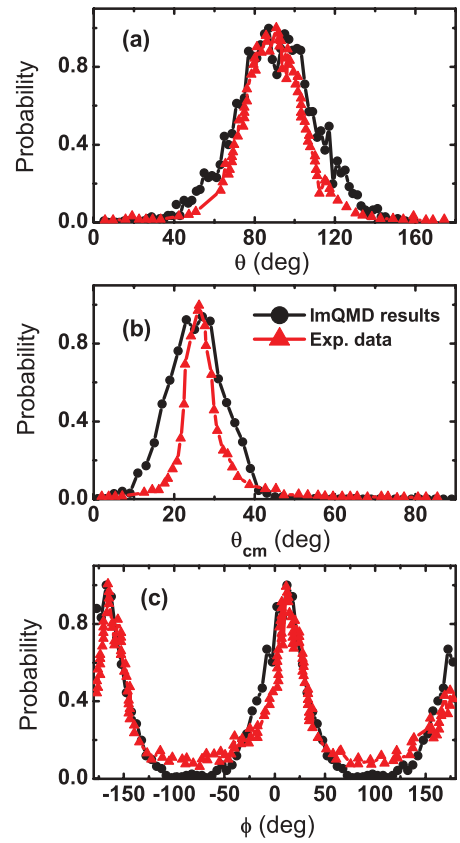

FIG. 9. (Color online) Angular distributions of fragments (a) out-of-plane angle θ, (b) $\theta_{\mathrm{c.m.}}$, and (c) azimuthal angle ϕ in cascade ternary reactions. The line with solid circles is the calculated results with the ImQMD model, and the line with triangles denotes experimental data [3]

also very helpful for understanding the mechanism of ternary breakup reactions. For the direct ternary process, the time interval t_{2-1} between the two separations is much smaller than 100 fm/c and we cannot show it here because the time interval for recording the position and momenta of particles is 100 fm/c in the calculations, given that the two separations happen almost simultaneously. So, in Fig. 11, we only show the distribution of time interval t_{2-1} for cascade ternary events at $b = 2, 7$, and 10 fm, respectively. The vertical axis is on a logarithmic scale. Investigating the slopes of the t_{2-1} distribution seems quite meaningful. In the central (or semicentral) collision case especially (see the top panel in Fig. 11), the decreasing slope of the t_{2-1} distribution obviously changes from the $t_{2-1} < 400$ fm/c region to the $t_{2-1} \geqslant 400$ fm/c region. The decreasing slopes for $t_{2-1} < 400$ fm/c for the $b = 2$ fm and $b = 7$ fm cases are almost the same, while the decreasing slope for $b = 10$ fm is much faster compared with the relatively small impact parameter cases. Does this change of the slope imply any change of the mechanism of the ternary breakup process? To answer this question, we investigate the configuration of the composite system before the first breakup takes place. It is found that for the ternary events with $t_{2-1} < 400$ fm, the composite systems generally have two preformed necks and form a three-body clusterization before the breakup, while for the ternary events with $t_{2-1} > 400$ fm/c there is only one preformed neck in the composite system, i.e., the two-body clusterization before the first breakup takes place. Thus, we can conclude that the ternary breakup events, including the direct ternary events and the cascade ones with $t_{2-1} < 400$ fm/c, originate from the composite systems with two preformed necks. For the ternary events stemming from the systems with only one preformed neck, the produced residue after the first breakup still takes time to rearrange particles to reach a lower energy state. Then, the residue continues to elongate, and finally breaks again (namely, the second breakup happens). For peripheral collisions, for example, at $b = 10$ fm (see the bottom panel in Fig. 11), the distribution of time interval t_{2-1} is sharply peaked at the very small value of t_{2-1}, which is only a binary process with neck emission.

D. The evolution of mass distributions of three fragments with impact parameter

From the previous discussion, we know that the time scales of the first and second breakup for direct and cascade ternary events are rather different at different impact parameter regions. The different time scales of the two separations in ternary breakup reactions must have an effect on their mass distributions. Figure 12 shows the mass distributions of fragments A_1, A_2, and A_3 for direct and cascade ternary events in $^{197}\mathrm{Au} + {}^{197}\mathrm{Au}$ at $15A$ MeV for impact parameters $b = 2$, 7, and 10 fm, respectively. The first row is for $b = 2$ fm case; the middle and third rows are for the $b = 7$ and 10 fm cases. The first, second, and third columns are for the distributions of A_1, A_2, and A_3, respectively. Let us first discuss the case of $b = 2$ fm. One sees from Fig. 12(b) that an evident

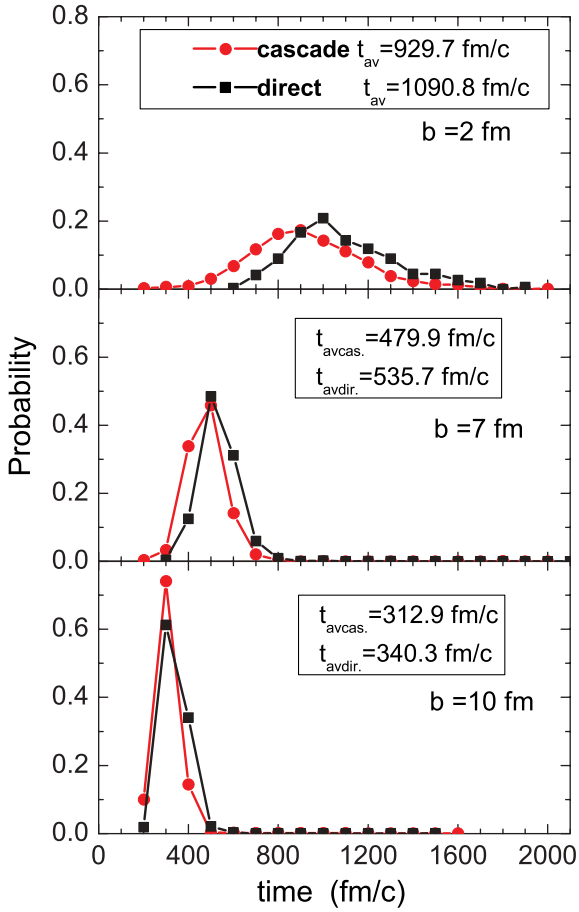

FIG. 10. (Color online) The distribution of the first separation time in ^{197}Au + ^{197}Au collisions at an energy of 15A MeV with $b = 2$, 7, and 10 fm.

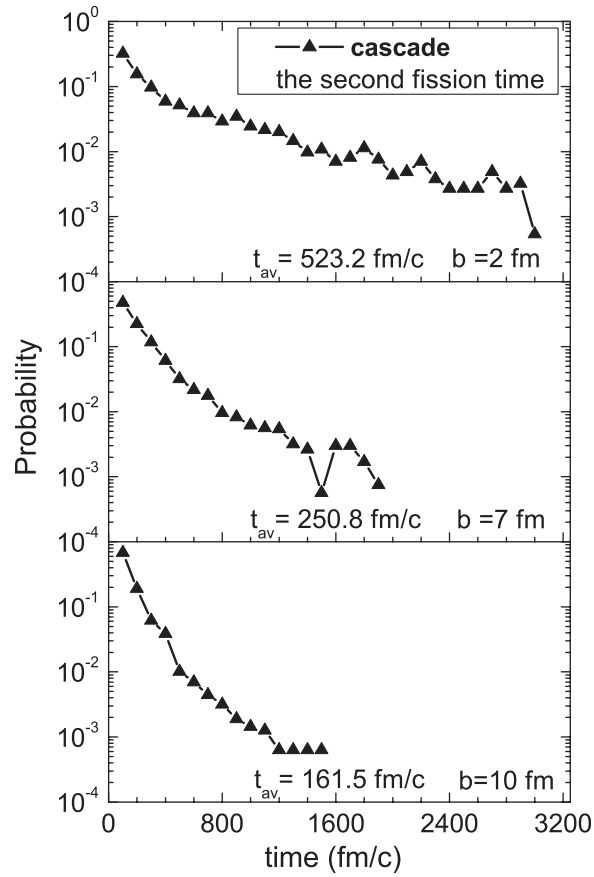

FIG. 11. The distribution of time interval t_{2-1} in cascade ternary events for ^{197}Au + ^{197}Au at 15A MeV with $b = 2$, 7, and 10 fm.

peak of mass distributions of A_2 appears at a mass number of around 120 for both direct and cascade ternary modes. Another feature shown in Figs. 12(a) and 12(c) is that the bumps of the A_1 and A_3 mass distributions appear at around $A \approx 140$ and $A \approx 90$. Those behaviors are similar for both cascade and direct ternary modes, but for the direct ternary case the bumps for A_1 and A_3 mass distributions deviate little from $A \approx 140$ and $A \approx 90$ and also there are relatively large fluctuations in the distributions because the reaction events are much less than those in the cascade case. The remarkable phenomena appearing in the A_1, A_2, and A_3 mass distributions at central collisions ($b = 2$ fm) are mainly related to the longer interacting time and strong dissipation between the projectile and target (as indicated in Figs. 10 and 11). They lead to a composite system reclustering and make it at a favorable configuration in energy. Now we turn to the second row in Fig. 12 for the case of $b = 7$ fm. The shapes of A_1, A_2, and A_3 mass distributions for cascade ternary events are similar to those at the $b = 2$ fm case, shown in the first row of Fig. 12, except they are a little wider. For direct ternary events, since the interacting time between the projectile and target is shortened, the bumps in the A_1 and A_2 mass distributions are moved to the larger mass side, i.e., the bump for the A_1 mass distribution is moved to around 180 [see Fig. 12(d)] and that for A_2 is moved to around 135 [see Fig. 12(e)]. The mass distribution for A_3 for the direct mode is slightly moved to the lighter mass side as compared with the cascade mode, which means that the binary breakup with neck emission slowly starts to play a role as the impact parameter becomes larger than 7 fm for the direct-mode ternary breakup process. For the peripheral collision case ($b = 10$ fm) the shapes of the A_1, A_2, and A_3 mass distributions, shown in the third row of Fig. 12, are considerably different from the cases of $b = 2$ fm and $b = 7$ fm. The mass distributions of A_1 and A_2 with peaks at around 190 and 170 become narrower for both direct and cascade ternary events. However, the mass distributions for cascade ternary events are a little wide and flat. The mass distribution of A_3 is peaked at small mass. Thus, from the mass distributions of fragments A_1, A_2, and A_3 at the $b = 10$ fm case, we can attribute A_1 and A_2 to the projectile-like (target-like) fragments and the third one is from the neck part. The reaction system only experiences a deep-inelastic reaction in this case.

E. The time evolution of rare shape configuration of the composite system in the ternary process

The possible space configurations of the composite system in the ternary process with three mass-comparable fragments are also important features for understanding the ternary

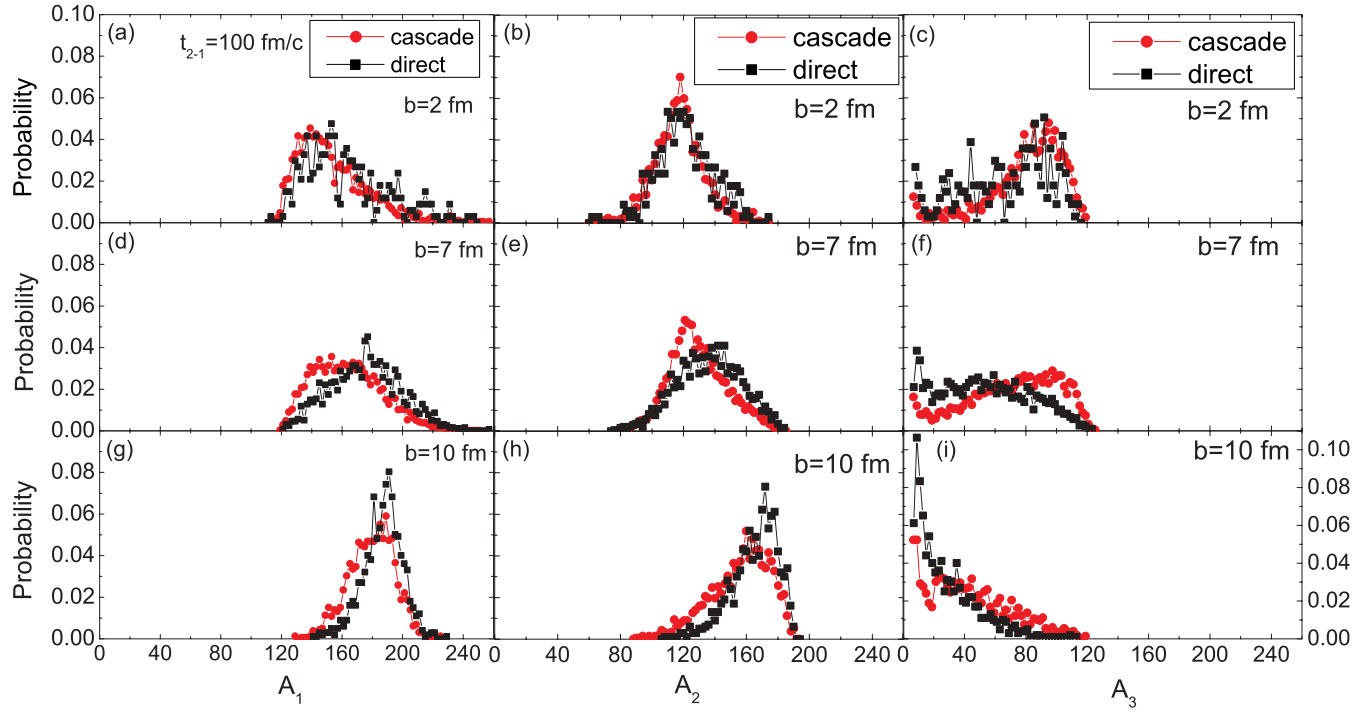

FIG. 12. (Color online) Mass distribution of three fragments A_1, A_2, and A_3 for ^{197}Au + ^{197}Au at 15A MeV with impact parameter $b = 2$, 7, and 10 fm, respectively.

dynamics. Within the microscopic transport model, we can dynamically illustrate the time evolution of those space configurations. As examples, in Figs. 5 and 6 we show the time-dependent pictures of two typical ternary events in ^{197}Au + ^{197}Au collisions at 15A MeV with impact parameters $b = 2$ and 7 fm, respectively. The shapes of the composite systems for these two events are both prolate elongated. The three fragments formed are emitted almost linearly. These are the most probable cases in the ternary breakup process with three mass-comparable fragments. However, in central reactions, say, $b = 2$ fm, we also find very rare events in which the composite systems can take a spherical-like configuration with small octuple deformation, in which case the three fragments formed are emitted in a triangular configuration. Figure 13 shows the time evolution of the shape configuration of the system for this typical event. One sees that at $t = 500$ fm/c the composite system with a roughly spherical shape is formed and then develops into a pear shape at 700 fm/c. At $t = 1100$ fm/c, one neck is formed. At about 1400 fm/c, the first time break takes place and the composite system divides into two parts. The larger part undergoes further elongation and eventually separates into two fragments again at 1600 fm/c. The lifetime of the composite system in these rare events is much longer than that in other cases. Although this kind of ternary events is very rare and only happens in central reactions, the special configuration and quite long lifetime of the formed composite systems are very interesting for some purposes, for example, for studies of exotic nuclear structure and spontaneous emission of positrons in strong electromagnetic fields.

V. SUMMARY

In summary, the ternary breakup of the very heavy system ^{197}Au + ^{197}Au at an energy of 15A MeV has been investigated by using the ImQMD model. We find that the calculation results can reproduce the characteristic features explored in a series of experiments; that is, the masses of three fragments are comparable in size and the very fast, nearly collinear breakup of the colliding system is dominant in the ternary breakup events. The study of the mechanism of ternary breakup shows that two kinds of modes exist: One is the direct mode for which the two time separations of the system happen almost simultaneously (the time interval between two separations being much less than 100 fm/c) and the other one is the cascade mode for which a two-step process is clearly shown. We then further study the evolution of the time scale of the first and the second separation with impact parameters in the ternary reactions. We find that the first separation happens about 50–100 fm/c later for the direct ternary mode as compared with the cascade ternary mode in central and semiperipheral reactions. The longer interaction time before the first separation in the direct ternary events in central or semicentral collisions allows the system to form a three-body cluster configuration, which is more favorable for reducing Coulomb repulsion. The evolution of the distribution of the time interval t_{2-1} between two time separations with impact parameter is also studied. We can roughly distinguish the events with $t_{2-1} < 400$ fm/c from those with $t_{2-1} \geqslant 400$ fm/c according to the slope of the distribution of t_{2-1} for central and semicentral reactions. For most of the events with $t_{2-1} <$ 400 fm/c for central and semicentral reactions, the two-neck (three-body-cluster) configuration is formed, but not for most

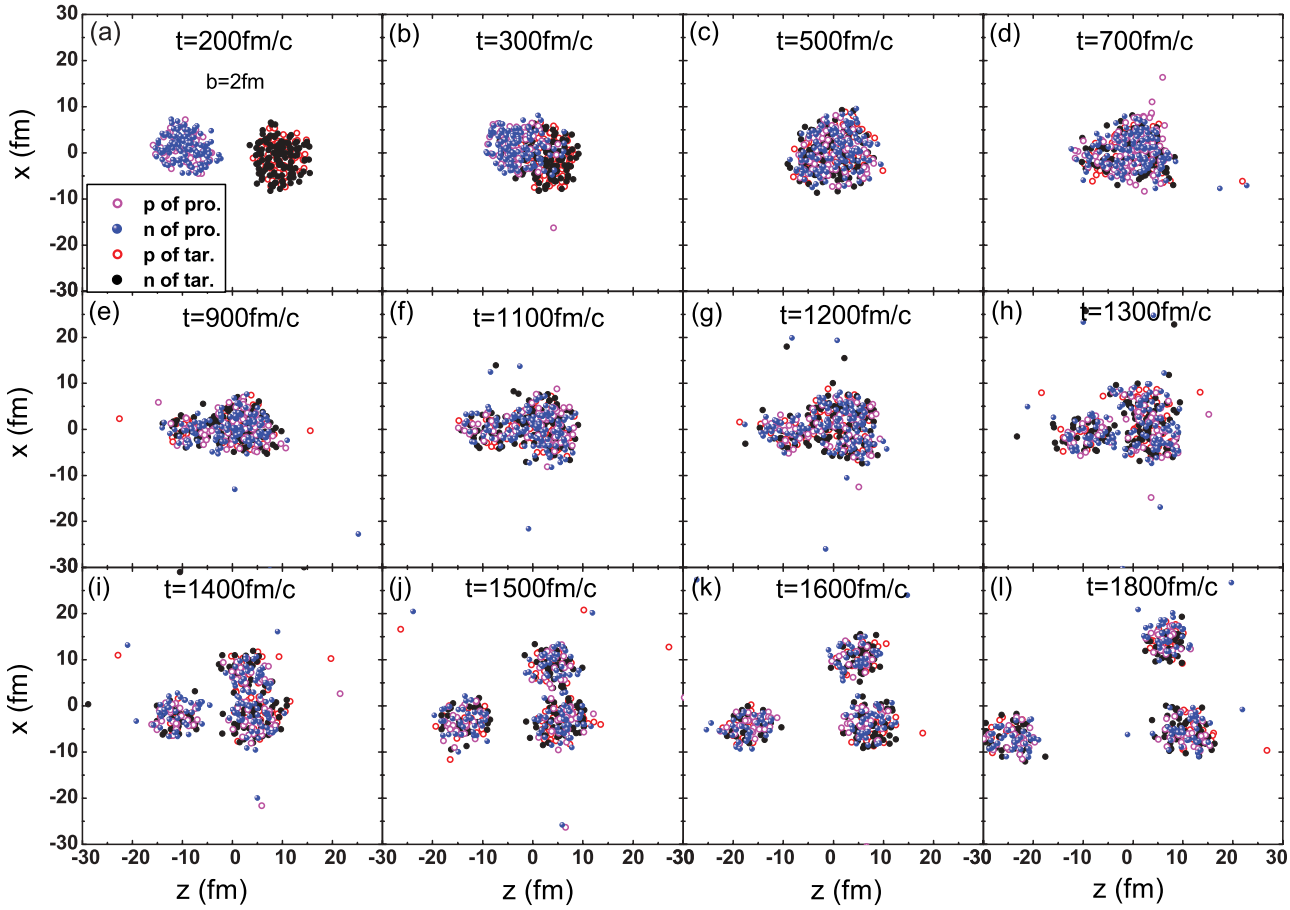

FIG. 13. (Color online) A typical ternary event for ^{197}Au + ^{197}Au at 15A MeV with $b = 2$ fm.

events with $t_{2-1} \geqslant 400$ fm/c. The mass distributions of three fragments at different impact parameters for two modes are also studied and show different breakup mechanisms from central and semicentral reactions to peripheral reactions. Our study shows that the ternary breakup events with the characteristic features found in a series of experiments mainly come from the breakup reactions at relatively small impact parameters. The peripheral reactions have a character of binary breakup with neck emission.

ACKNOWLEDGMENTS

J.L.T. is grateful to Professor N. Wang for fruitful discussions. This work is supported by the National Natural Science Foundation of China (Grants No. 10675172, No. 10875031, No. 10975095, No. 10905021, and No. 10975019), National Basic Research Program of China (Grant No. 2007CB209900), and the Scientific Research Foundation for the Returned Overseas Chinese Scholars, Ministry of Personnel (Grant No. MOP2006138).

[1] I. Skwira-Chalot *et al.*, Int. J. Mod. Phys. E **15**, 495 (2006); **16**, 511 (2007).
[2] I. Skwira-Chalot *et al.*, Phys. Rev. Lett. **101**, 262701 (2008).
[3] J. Wilczynski *et al.*, Int. J. Mod. Phys. E **17**, 41 (2008).
[4] J. Wilczynski *et al.* Phys. Rev. C **81**, 067604 (2010).
[5] X. Wu, J. A. Maruhn, and W. Greiner, J. Phys. G **10**, 645 (1984); X. Wu, K. Depta, R. Herrmann, J. A. Maruhn, and W. Greiner, IL Nuovo Cimento A **87**, 309 (1985).
[6] N. Carjan, K. Siwek-Wilczynska, and I. Skwira-Chalot, Int. J. Mod. Phys. E **17**, 53 (2008).
[7] Y. Zhang *et al.*, Phys. Lett. B **664**, 145 (2008).
[8] M. B. Tsang, Y. Zhang, P. Danielewicz, M. Famiano, Z. Li, W. G. Lynch, and A. W. Steiner,Phys. Rev. Lett. **102**, 122701 (2009).
[9] N. Wang, Z. Li, and X. Wu, Phys. Rev. C **65**, 064608 (2002).
[10] N. Wang, Z. Li, X. Wu, J. Tian, Y. X. Zhang, and M. Liu, Phys. Rev. C **69**, 034608 (2004).
[11] N. Wang *et al.*, Mod. Phys. Lett. A **20**, 2619 (2005).
[12] J. Tian, X. Wu, K. Zhao, Y. Zhang, and Z. Li, Phys. Rev. C **77**, 064603 (2008).
[13] K. Zhao, X. Wu, and Z. Li, Phys. Rev. C **80**, 054607 (2009).
[14] C. Hartnack *et al.*, Nucl. Phys. A **495**, 303 (1989).

[15] J. Aichelin, Phys. Rep. **202**, 233 (1991), and references therein.
[16] Ch. Hartnack, R. K. Puri, and J. Aichelin, Eur. Phys. J. A **1**, 151 (1998).
[17] A. Ono, H. Horiuchi, T. Maruyama, and A. Ohnishi, Phys. Rev. Lett. **68**, 2898 (1992); Y. Kanada En'yo and H. Horiuchi, Phys. Rev. C **52**, 647 (1995).
[18] H. Feldmeier and J. Schnack, Rev. Mod. Phys. **72**, 655 (2000).
[19] M. Papa, T. Maruyama, and A. Bonasera, Phys. Rev. C **64**, 024612 (2001).
[20] H. Kruse, B. V. Jacak, J. J. Molitoris, G. D. Westfall, and H. Stocker, Phys. Rev. C **31**, 1770 (1985).
[21] F. S. Zhang, L. W. Chen, Z. Y. Ming, and Z. Y. Zhu, Phys. Rev. C **60**, 064604 (1999).
[22] Q. Li and Z. Li, Mod. Phys. Lett. A **17**, 375 (2002).